JOURNAL OF MATERIALS SCIENCE 26 (1991) 5777–5792

Cooling rate effects on acoustic emission-microstructure relationships in ferritic steels

H. N. G. WADLEY*, C. B. SCRUBY
AEA Industrial Technology, Harwell Laboratory, Oxon, OX11 0RA, UK

The study reported here systematically investigates the nature of the relationship between defect dynamics and acoustic emission in specially prepared low alloy steels containing 3.25 wt% Ni, 1 wt% Mn with carbon contents between 0.06 to 0.49 wt% as the rate of cooling from the austenitic state is varied. During plastic flow, the strongest acoustic emissions are generated from slowly cooled microstructures with a $\geqslant 10$ μm ferrite dimension, a low initial dislocation density and very widely spaced precipitates. This emission is believed to originate from the propagation of high velocity ($>100\ ms^{-1}$) dislocation groups in the ferrite phase. It is consistent with an emission model in which the product of the dislocation glide distance and velocity (which are both controlled by microstructure) determines the amplitude of the acoustic emission. In air cooled samples containing retained austenite, additional emission is seen and suggests that stress-induced martensitic transformations are a second emission source. During subcritical microfracture, intergranular and alternating shear modes of microcracking occur in high strength conditions and generate strong signals. Both mechanisms involve the rapid propagation of cracks over distances of 10–100 μm and the resulting emission is consistent with the model predictions. The ductile dimple mode of fracture is found to generate no detectable signals regardless of dimple spacing and fracture stress, which is consistent with the view that such fracture occurs under essentially quasi-static conditions with little or no mechanical instability.

1. Introduction

Acoustic emission is the term used for the elastic waves generated by moving cracks and dislocations in solids [1]. The waves are generated by local stress redistributions associated with the motion of dislocations and cracks in a stressed solid. In solids, both longitudinal and transverse elastic waves can be generated by the action of an abrupt local force (induced for example by a moving dislocation or growing crack); they propagate spherically away from the source and, upon arriving at a free surface, cause both transient and static displacements [2]. The static component of displacement can be measured with strain gauges in the conventional way. This has enabled a reasonable understanding of the link between microstructure-static mechanical properties to be developed. The transient displacements (acoustic emission) have only more recently begun to be measured; their measurement promises to provide a better understanding of the dynamics of dislocation and fracture processes [3].

Analogous relationships between microstructure and dynamic mechanical properties should exist for the kinematical aspects of deformation and fracture. Thus, it is observed that the intensity of acoustic emission signals (in a given frequency window) is highly sensitive to microstructure, presumably because the microstructure controls the velocities and distances that dislocations and cracks propagate, and these are the factors controlling the redistribution of force, and therefore the acoustic source [4]. The weakness of techniques for observing these effects in the past has contributed to a relative lack of progress in defect dynamics. A major reason for the work here is to establish better experimental insights into the dynamics of deformation and fracture in model low alloy steels.

A second reason for this study is that the acoustic emission technique can be used for non-destructive evaluation during either materials processing or proof testing, or while components are in use [5, 6]. The ability of the technique to locate remotely the site of active defects is a unique feature of the method; as is its sensitivity to only those defects that actually grow under service loads (the technique is insensitive to flaws that are not critically stressed). However, the application to some structural materials, particularly steels, has been severely hampered by the discovery that some processes of deformation/fracture are undetectable [7]. In particular, the acoustic signals associated with ductile fracture are so weak that they are obscured by background noise. Subsequent work has

* *Present address*: Department of Materials Science/Mechanical and Aerospace Engineering, Thornton Hall, University of Virginia, Charlottesville, VA 22903-2442 USA.

0022–2461/91 $03.00 + .12

TABLE I Chemical composition of steels used for acoustic emission study

Element (wt %)	C	N	O	S	P	Ni	Mn	Si	Cu
Steel D	0.060	0.003	0.003	0.0059	< 0.005	3.22	1.06	0.51	0.02
Steel E	0.169	0.003	0.003	0.0059	< 0.006	3.30	1.03	0.51	0.01
Steel F	0.486	0.003	0.003	0.0059	< 0.101	3.44	1.08	0.49	0.02

Note: Cr, Mo, Al, Ti, V, Co, Zn, As, Zr, Nb, Sn, Bi are all less than 0.01 wt %.

confirmed that microstructure has a strong effect upon the amplitude of acoustic emission accompanying flaw growth. The origin of this effect lies in the emerging understanding of the relationships between defect dynamics and microstructure.

Since many flaws reside in or near welds where there exist strong microstructural variations, it is essential to understand the acoustic emission-microstructure relationship for a particular class of materials if the reliability of the technique for flaw detection is to be established *a priori*. In the work reported here, we have attempted to do this by systematically investigating the influence of microstructure on the micromechanism of deformation/fracture and the generation of acoustic emission.

The approach we adopt involves the preparation of high purity steels, designed on the one hand to manifest the features of typical structural steels, while on the other, allowing controlled variation of the microstructure. The paper reports the effect of varying the cooling rate (after a standard austenization heat treatment) upon acoustic emission and mechanical properties. This enables the study of a wide range of microstructures that might be encountered near a weld. Subsequent papers will investigate the effects of tempering, of higher concentrations of sulphide inclusions, and inclusion morphology and orientation.

2. Materials

For the purposes of this work it was considered necessary to prepare special low alloy steels to control the level of impurities (which are known to influence mechanical properties and acoustic emission response) and to facilitate microstructure manipulation. To this end, three high purity vacuum melted ingots of nominally 3.25 wt % Ni-1 wt % Mn steel were produced. The ingots had a low sulphur content (0.006 wt % S) and consequently contained relatively few MnS inclusions. The carbon concentrations of the steel sets were nominally 0.06, 0.18 and 0.49 wt %.

Ingots, each weighing 150 kg, were prepared from Japanese electrolytic iron using a vacuum melting technique. Each ingot had a cross-section of ~15 mm × 150 mm and a length of ~ 600 mm. The steel was silicon deoxidized, alloyed with Mn (which combined with the sulphur to form sulphide inclusions), and Ni (to give good hardenability and thus homogeneous microstructures in quenched samples). The chemical composition of the ingots was determined on 2-cm cube samples cut from five widely different locations within each ingot. These multiple analyses were made in order to check for possible macrosegregation of alloying elements and thus potential sample-to-sample compositional variations. Composition varied by less than 10 per cent between samples: the average of the five compositions for each alloy are given in Table I.

A billet approximately 150 mm in length was cut from each ingot. These billets were hot forged to weld together minor casting defects such as microporosity, to improve chemical homogeneity and to control the sulphide morphology. For the tests reported here on lower sulphur material, we wished to ensure that the inclusions had small aspect ratios. This was achieved by using a high working temperature ($\approx$ 1200 °C), so that the steel was more deformable than the inclusions, and a small forging reduction (3:1). In practice, the forging treatment involved coating the billets with a glass powder (to reduce oxidation and to act as a lubricant during forging). The billets were press-forged from an initial cross-section of 150 × 150 mm to an intermediate slab cross-section of 90 × 135 mm. They were then reheated to 1200 °C and forged to a final cross-section of 300 × 50 mm. This resulted in a small ($\approx$ 2:1) inclusion elongation along the prior ingot axis.

Cylindrical dumbbell tensile specimens were machined from the forged plates with their tensile axis parallel with the prior ingot axis. The gauge length and diameter were 40 and 3 mm, respectively. Groups of four or five specimens from each ingot were subjected to identical heat treatments so that multiple tests of a given condition could be made.

3. Heat treatments

The groups of samples of each steel were all austenitized at 1000° ± 5 °C for one hour in argon and then cooled at varying rates by:

1. Ice brine quenching
2. Water (at 22 °C) quenching
3. Oil quenching
4. Air cooling (normalizing) at approximately 200 °C min^{-1}
5. Furnace cooling at 30 °C/h (Furnace cool I)
6. Furnace cooling at 10 °C/h (Furnace cool II).

4. Experimental procedure

Identical techniques and procedures to those reported in [8] were used for the testing of the samples reported here. To reduce the anticipated effects of scatter between acoustic emission measurements of nominally identical samples, tests were carried out on three or four samples and average values are reported.

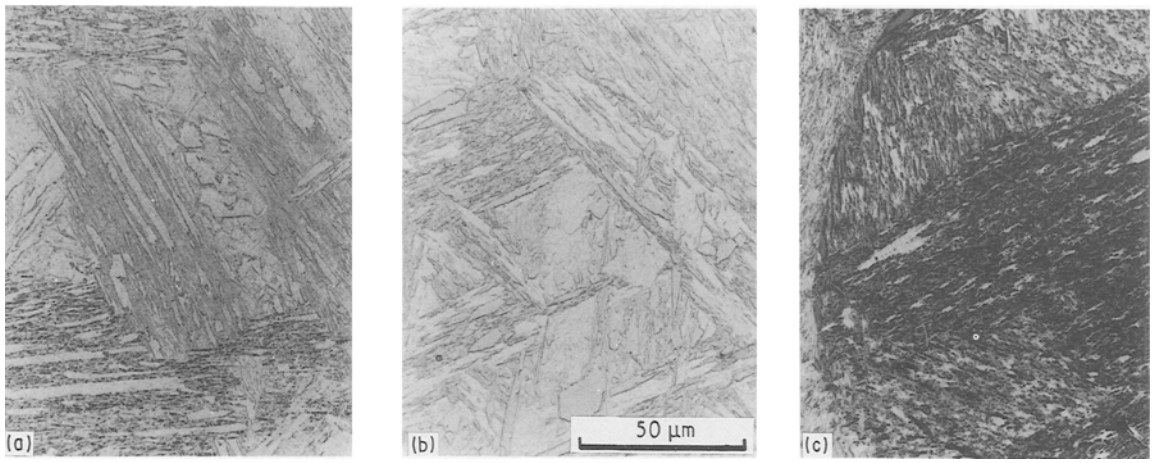

Figure 1 Effect of carbon concentration on the microstructure of ice brine quenched specimens.

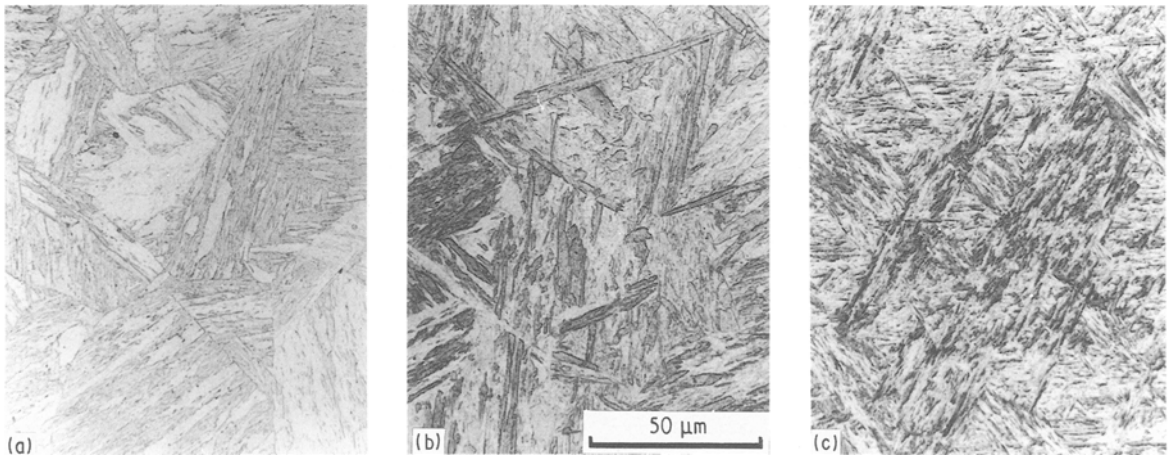

Figure 2 Effect of carbon concentration on the microstructure of oil quenched specimens.

One additional sample, representative of each treatment, was used to make accurate mechanical property measurements using a computer-controlled testing machine under closed-loop servohydraulic control.

5. Results

We consider separately the microstructure, acoustic emission results, mechanical properties and fracture characteristics for the range of microstructures studied.

5.1. Microstructural characterization

The iced brine (Fig. 1), water and oil (Fig. 2) quenches produced almost identical martensitic microstructures in steels D, E and F. Rather large carbides were observed in isolated areas (e.g., Fig. 1a and Fig. 2a) in the low and to a lesser extent, medium carbon steels. These were not uniformly distributed and are considered an autotempering produce thought to have nucleated in the martensite laths that formed first (at highest temperature) during cooling. These could have been in regions of microsegregation with locally low carbon and/or alloy element content (and thus relatively higher M_s temperature).

Transmission electron microscopy (TEM) of the oil-quenched samples (Fig. 3) indicated the presence of a dense dislocation structure, a few large plate-like carbides in steels D and E, and fine carbides in a twinned martensite in steel F. The transformation-induced dislocations are clearly resolvable in Fig. 3a. While it was difficult to resolve these dislocations in the other steels, it is well known that their density increases with carbon concentration. The plate-like carbides in steels D and E were 100–500 nm long, and non-uniformly distributed (i.e., they were only present in some martensite laths) in agreement with optical microscopy. The carbides in steel F were much smaller (3–10 nm) and more uniformly distributed (Fig. 3c), and are possibly ε-carbides. Small (2–5%) fractions of retained austenite were present. No attempt to quantify the volume fraction of retained austenite was made, but the greatest concentration would be expected in steel F with the lowest M_s temperature.

Air cooling, Fig. 4, resulted in widely differing microstructures for the three steels. In steel D, a duplex structure formed consisting of ferrite and a "blocky" retained austenite. The ferrite had a lath morphology with dimensions comparable to the prior austenite grain size (30 μm). Regions of retained austenite were up to 10 μm in dimension. The medium

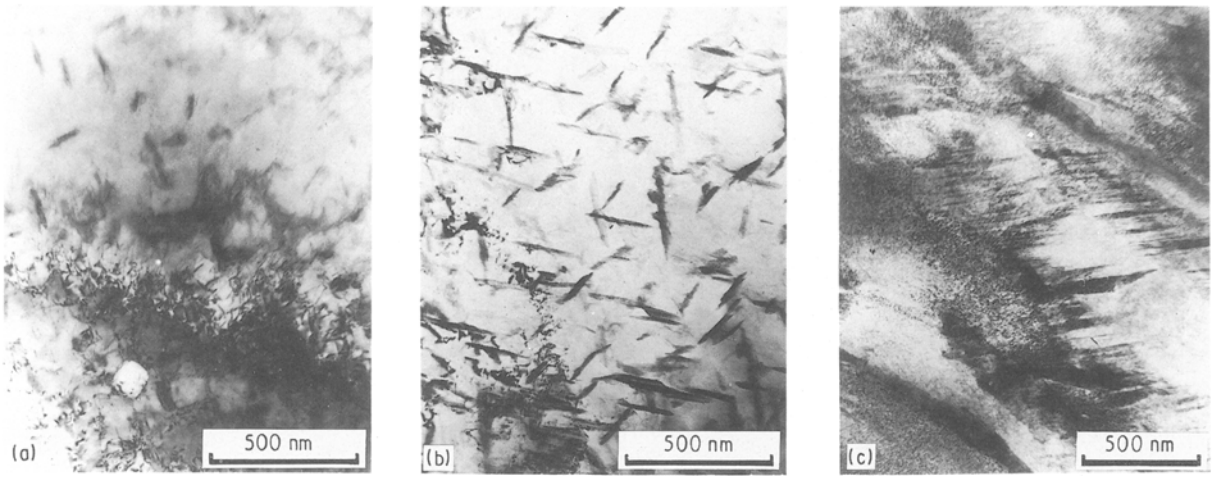

Figure 3 Transmission electron micrographs of oil quenched samples.

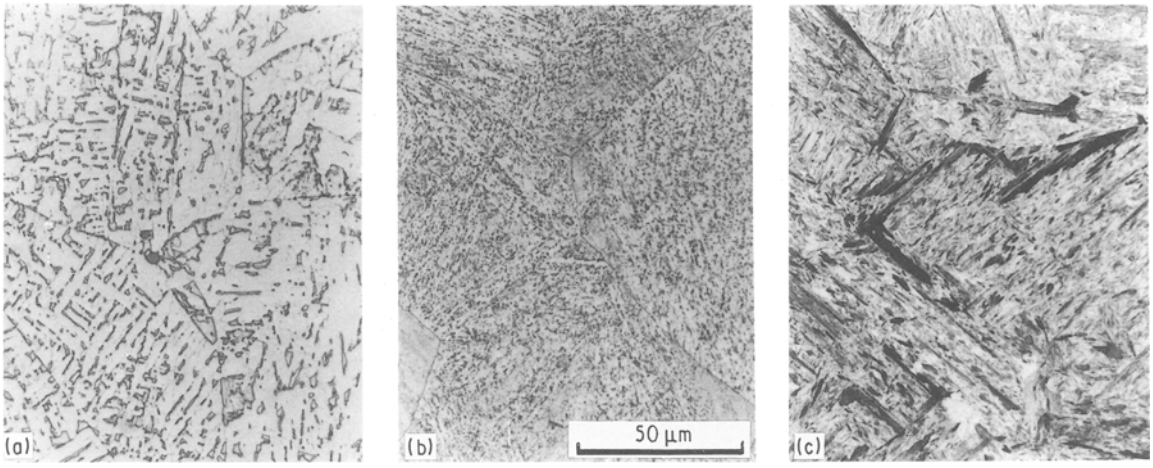

Figure 4 Effect of carbon concentration on the bainitic microstructures of air cooled specimens.

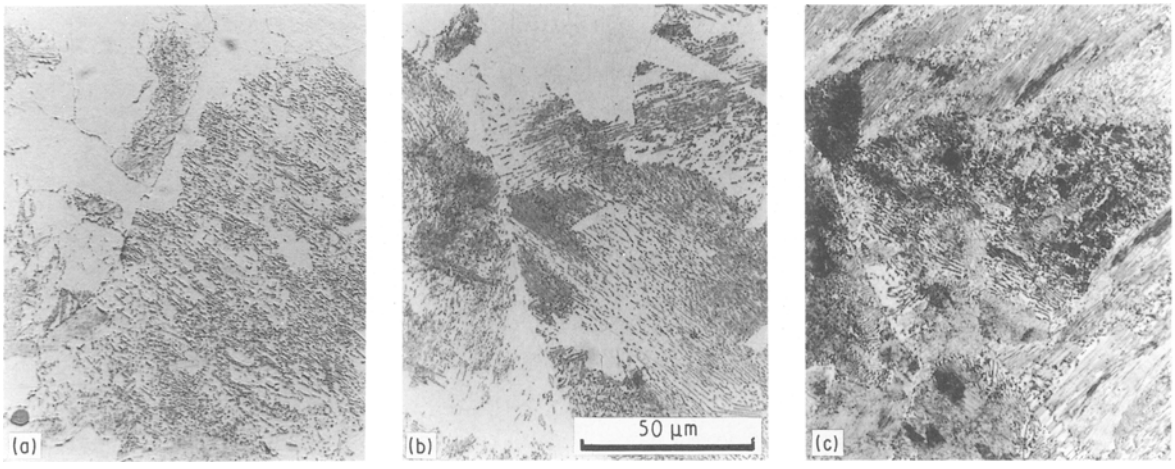

Figure 5 Effect of carbon concentration on the ferritic/pearlitic microstructures on furnace cooled specimens ($10\,^{\circ}C\,h^{-1}$).

carbon steel, Fig. 4(b), transformed to an upper bainite. The carbides in this sample were quite coarse and spheroidal, indicating appreciable post-transformation coarsening. The high carbon alloy, Fig. 4(c), had an acicular structure containing darkly etched regions indicating extensive carbide precipitation and appears to be a form of lower bainite. Comparison of Fig. 4b and c shows a significant difference in the intercarbide spacing.

Furnace cooling led to a ferrite-pearlite microstructure in all three alloys (Fig. 5). We observed an increase in pearlite volume fraction (> 90% in steel F) and a decrease in cementite interlamellar spacing with increase in carbon content that were both greater than

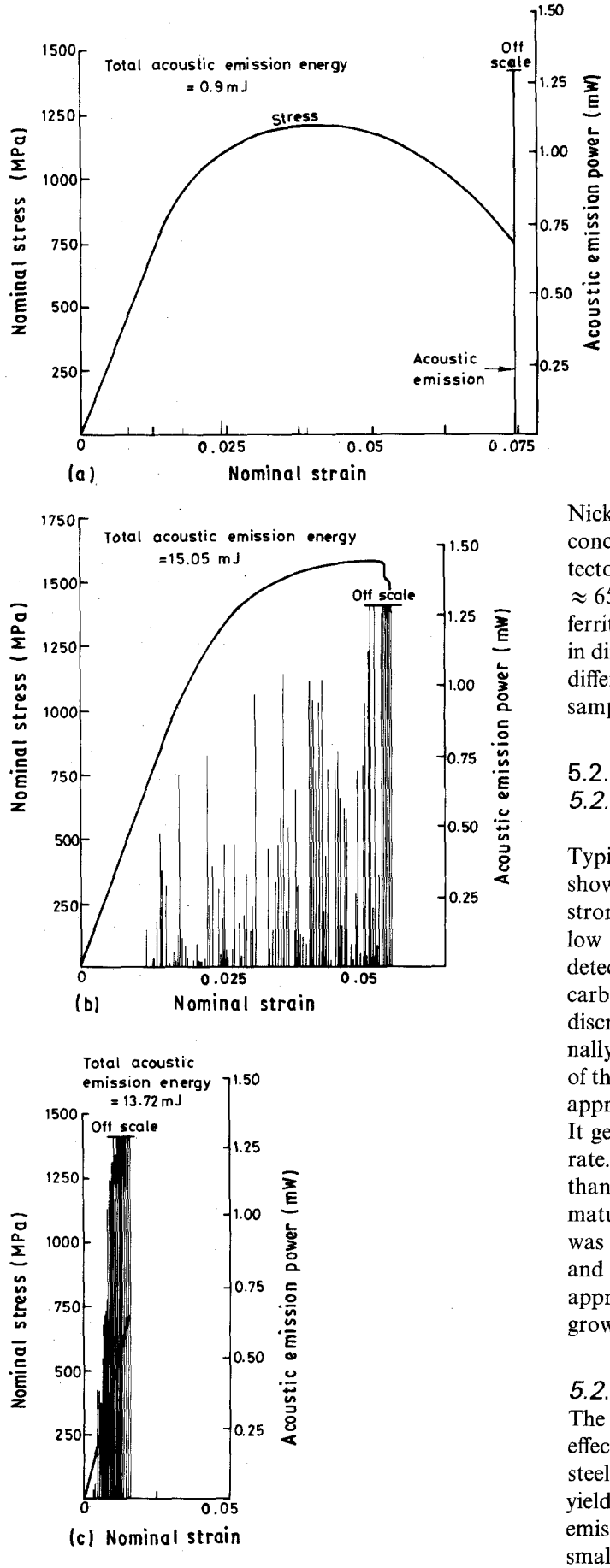

Figure 6 Acoustic emission as a function of nominal strain for water quenched steels (a) D; (b) E and (c) F.

predicted for a plain carbon steel. The increased pearlite fraction is believed to be due to the reduction in eutectoid carbon concentration by the alloy elements. Nickel in this alloy, for example, reduces the eutectoid concentration from ≈ 0.8 wt % to 0.65 wt % (the eutectoid temperature is also reduced from 723° to ≈ 650°C). In the high carbon alloy, pro-eutectoid ferrite was restricted to a few isolated islands 5–10 μm in dimension. There was no observable microstructural difference at optical microscope resolution between samples cooled at the two furnace cooling rates.

5.2. Acoustic emission measurements

5.2.1. Iced-brine and water quenched conditions

Typical acoustic emission data for the three steels are shown in Fig. 6. Carbon concentration clearly has a strong effect upon the acoustic emission activity. The low carbon steel, (Fig. 6a), generated virtually no detectable acoustic emission. In contrast, the medium carbon steel, Fig. 6b, started to generate a series of discrete, individually energetic signals in the nominally elastic region during micro-yield. The intensity of these signals tended to increase as final fracture was approached. The high carbon steel, Fig. 6c, was brittle. It generated numerous discrete signals at a very high rate. It generated slightly less total emission energy than the medium carbon steel only because of premature fracture: the acoustic emission per unit strain was much greater. The emission power of the medium and high carbon samples increased as final fracture approached a feature well suited for reliable crack growth detection.

5.2.2. Oil quenched condition

The (slightly slower) oil quench only had a very small effect on the acoustic emission from the low carbon steel, just a few weak signals were emitted near general yield (Fig. 7a). There was a very large reduction in emission from the medium carbon steel, Fig. 7b, and a smaller reduction from high carbon steel, Fig. 7c. In the high carbon steel it was noted that the emission still increased with the approach of final fracture. It was also noted that the emission near yield in steels D and E consisted of many individually low energy emission signals that overlapped each other. On an oscilloscope they gave the appearance of a rise in

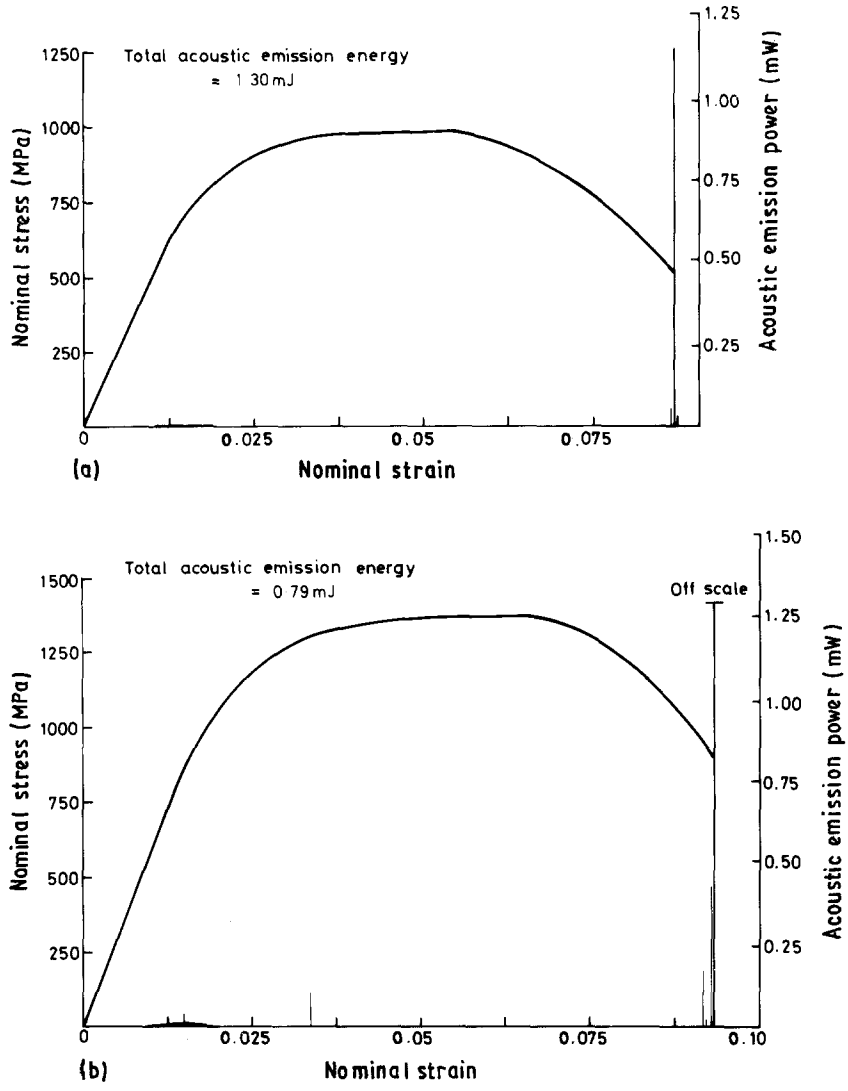

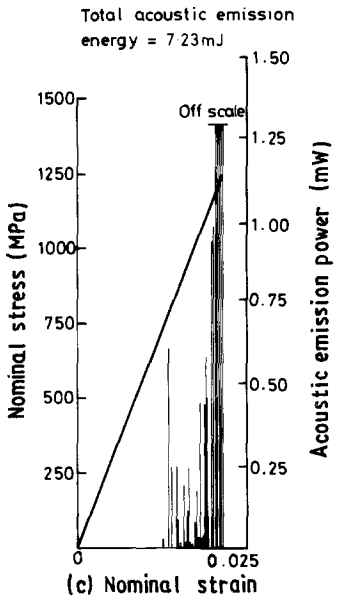

Figure 7 Acoustic emission as a function of nominal strain for oil quenched steels (a) D; (b) E and (c) F.

background electronic noise and are referred to in the literature as "continuous" emission.

5.2.3. Air cooled condition

The low carbon steel, with the duplex structure discussed above, generated a very large number of overlapping emissions giving the highest total acoustic emission energy observed in any test (Fig. 8a). Their rate went through a maximum close to general yield. Emission with similar characteristics to this, but with much less total energy, was also observed in the medium carbon steel. Here, however, the peak in activity occurred at a lower strain, in the microstrain region before general yield. In the high carbon steel there was an even smaller emission peak in the nominally elastic region. In the fracture region the emission from the high carbon steel (F) was further reduced compared with faster quenched materials.

5.2.4. Slow cooled conditions

The low and medium carbon steels again generated emission during the initial yielding of a sample (Fig. 9a and b). In contrast to air cooled material the emission activity was significantly smaller and was linked to the appearance of a plateau on the stress–strain curve, which is associated with the nucleation and propagation of Luders bands. In the medium carbon steel the peak at general yield was smaller than that of the low carbon steel. The emission in the high carbon steel was even less than that of medium carbon material, and was also very much less than that for the

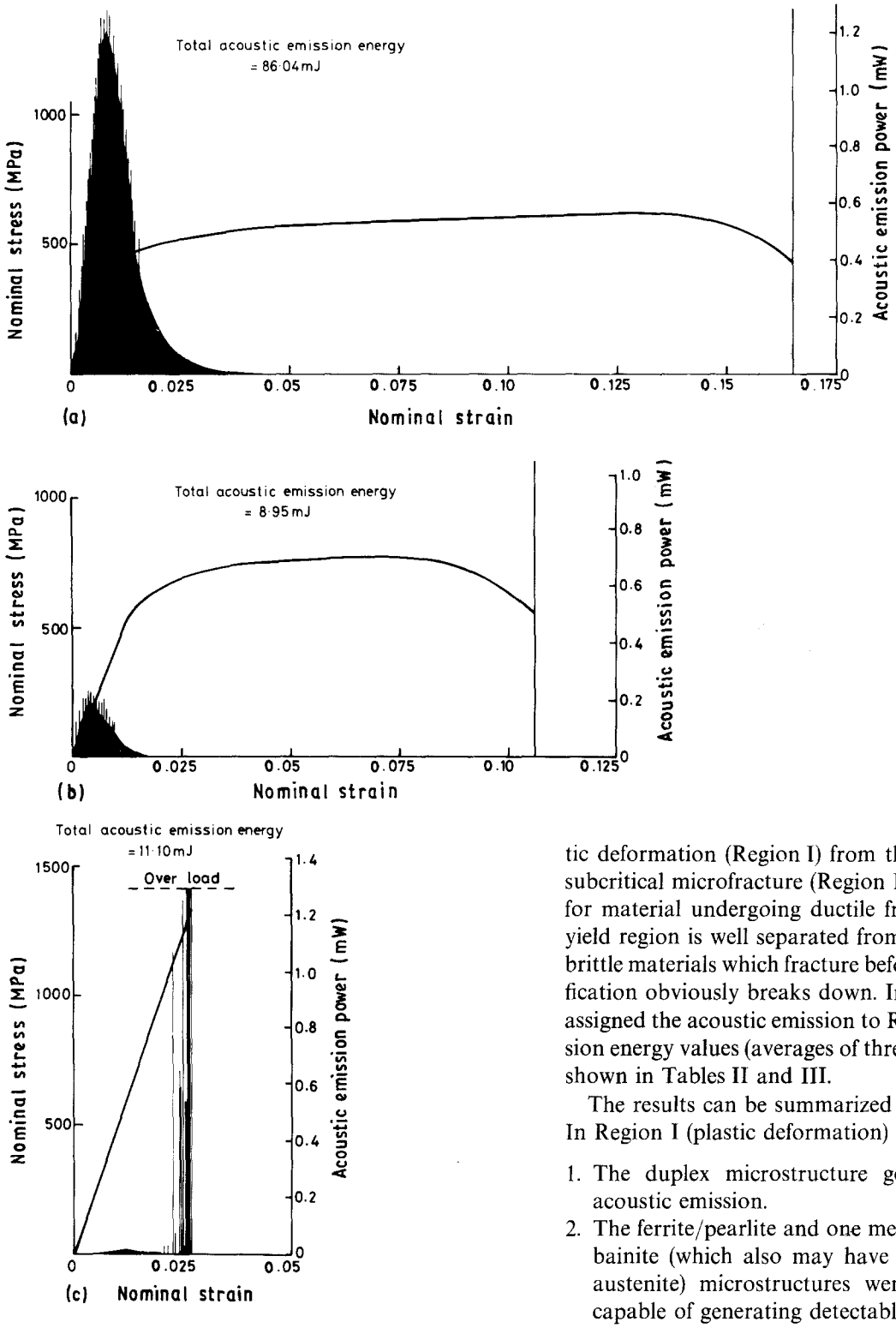

Figure 8 Acoustic emission as a function of nominal strain for air cooled steels. (a) D; (b) E and (c) F.

other heat treatments of high carbon steel (Fig. 9c). The loss of fracture-related acoustic emissions following slow cooling correlated with a transition from brittle to ductile fracture behaviour. For comparison purposes, we calculated the acoustic emission energy (the integrated acoustic emission power) detected in two regions of the stress–strain curve: Region I – zero to maximum nominal stress and Region II- maximum nominal stress to final fracture.

The objective of these classifications is to separate the acoustic emission due mostly to yield region plastic deformation (Region I) from that associated with subcritical microfracture (Region II). This works well for material undergoing ductile fracture because the yield region is well separated from fracture. For very brittle materials which fracture before yield, this classification obviously breaks down. In this case we have assigned the acoustic emission to Region II. The emission energy values (averages of three or more tests) are shown in Tables II and III.

The results can be summarized as follows:
In Region I (plastic deformation)

1. The duplex microstructure generated the most acoustic emission.
2. The ferrite/pearlite and one medium carbon upper bainite (which also may have contained retained austenite) microstructures were the only others capable of generating detectable emission.

TABLE II Plastic deformation generated acoustic emission (region I)

Heat treatment	Acoustic emission energy $m^{-1} J^{-1}$		
	Steel D	Steel E	Steel F
Ice brine quench	0.09	a	a
Water quench	0.43	a	a
Oil quench	1.35	0.04	a
Air cool	85.59	8.43	2.0
Furnace cool 30 °C h^{-1}	37.36	21.21	0.77
Furnace cool 10 °C h^{-1}	5.71	0.89	0.59

* Indicates fracture before yield. Acoustic emission included in data for Region II.

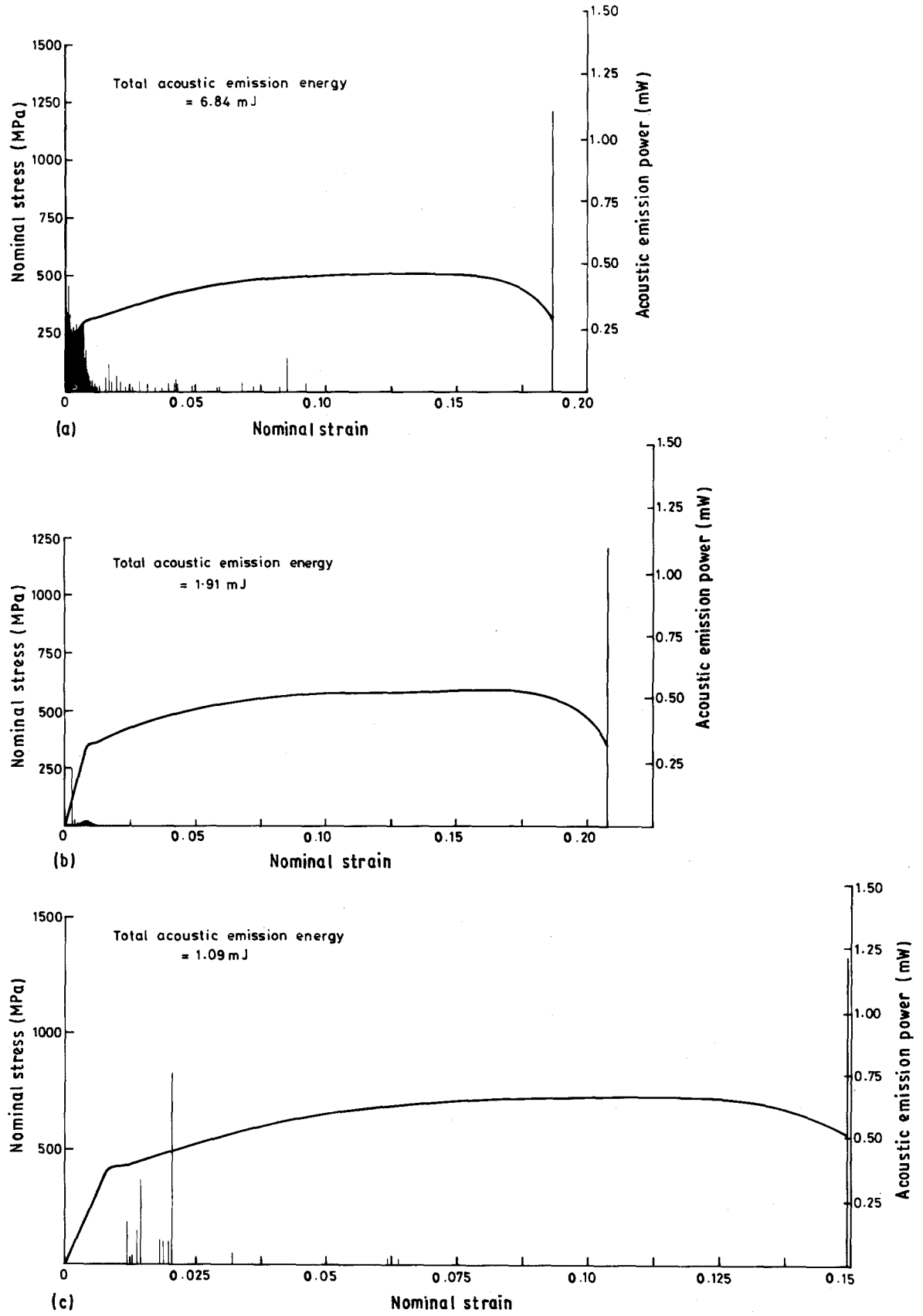

Figure 9 Acoustic emission as a function of nominal strain for steels furnace cooled at $\approx 10\,^{\circ}C\,h^{-1}$, where (a) is Steel D; (b) is E and (c) is F.

3. Detectable acoustic emission decreased with increasing carbon concentration for the same heat treatment. The emission was initiated during microyield and went through a maximum in rate close to general yield. For slow-cooled ferritic-pearlite microstructures, the acoustic emission was closely associated with the nucleation and propagation of Luder's bands.

In Region II (microfracture)

1. The martensitic microstructures generated the most acoustic emission.

TABLE III Fracture generated acoustic emission (region II) acoustic emission energy/mJ

Heat treatment	Acoustic emission energy (mJ)		
	Steel D	Steel E	Steel F
Ice brine quench	0.63	4.53	22.65
Water quench	0.60	8.26	19.51
Oil quench	0.50	0.70	6.66
Air cool	0.45	0.52	9.10
Furnace cool 30 °C h^{-1}	0.28	0.37	0.47
Furnace cool 10 °C h^{-1}	0.38	0.34	0.50

2. The acoustic emission energy increased with carbon concentration (degree of brittle behaviour) for a given heat treatment. The signals from microfracture tended to increase both in energy and rate of occurrence (number per unit strain) as final fracture was approached. The individual signals were usually more energetic than those generated in Region I.

5.3. Mechanical properties

Digital load-displacement records for samples of each heat treatment were analysed to obtain parameters of the stress–strain behaviour such as the 0.1 and 0.2 per cent proof stresses (σ_{uts}) and strain to maximum stress. The index of ductility taken was the plastic extension to failure. The work-hardening behaviour was characterized by the values of the work-hardening rate at 1 and 5 per cent strain. These data are summarized in Table IV. The yield and ultimate tensile stress increased with both increased cooling rate and carbon concentration. Ductility exhibited the inverse behaviour. Low strain (1%) work-hardening decreased with decreasing cooling rate. For a given heat treatment, the rate was higher for higher carbon content alloys.

5.4. Fractography

Scanning electron microscopy (SEM) was used to characterize the fracture mode of representative acoustic emission test samples. Three types of fracture; cleavage, alternating shear, and ductile-dimple, were observed. Their correlation with heat treatment and carbon concentration is summarized in Table V. Examples of each are shown in Fig. 10. At the microscopic level, the fracture behaviour of the steels was quite sensitive to heat treatment. In steel D, Fig. 11, the fracture surface was covered with dimples; the

TABLE IV Mechanical properties for steels D, E and F as a function of quench rate

Treatment	$\sigma_{0.1}$ (MPa)	$\sigma_{0.2}$ (MPa)	σ_{uts} (MPa)	Strain to UTS	Ductility (mm^{-1})[a]	Work-hardening (Rate/GPa)
Steel D						
Ice brine quench	647	776	1008	0.029	2.90	19.6
Water quench	651	751	985	0.028	2.61	19.1
Air cool	376	430	566	0.067	5.69	5.4
Furnace cool I	295	307	513	0.159	9.24	4.6
Furnace cool II	305	305	476	0.162	8.53	3.8
Steel E						
Ice brine quench	855	971	1368	0.025	2.01	28.1
Water quench	885	968	1416	0.046	1.89	29.7
Oil quench	759	878	1333	0.042	3.17	28.9
Air cool	700	798	1004	0.014	3.27	–
Furnace cool I	355	372	595	0.130	5.09	5.4
Furnace cool II	340	351	565	0.147	8.21	4.8
Steel F						
Ice brine quench	–	–	403	0.003	0.35	–
Water quench	–	–	659	0.004	0.32	–
Oil quench	–	–	1101	0.008	0.72	–
Air cool	676	778	1528	0.053	1.11	25.4
Furnace cool I	460	474	809	0.104	5.49	8.9
Furnace cool II	438	442	789	0.104	5.71	9.1

[a] 4 cm gauge length.

TABLE V Fracture behaviour of low sulphur steel

	Steel D	Steel E	Steel F
Ice brine quench	Ductile-dimple	Alternating shear	Cleavage
Water quench	Ductile-dimple	Alternating shear	Cleavage
Oil quench	Ductile-dimple	Ductile-dimple	Cleavage
Air cool	Ductile-dimple	Ductile-dimple	Quasi-cleavage
Furnace cool (fast)	Ductile-dimple	Ductile-dimple	Alternating shear
Furnace cool (slow)	Ductile-dimple	Ductile-dimple	Alternating shear

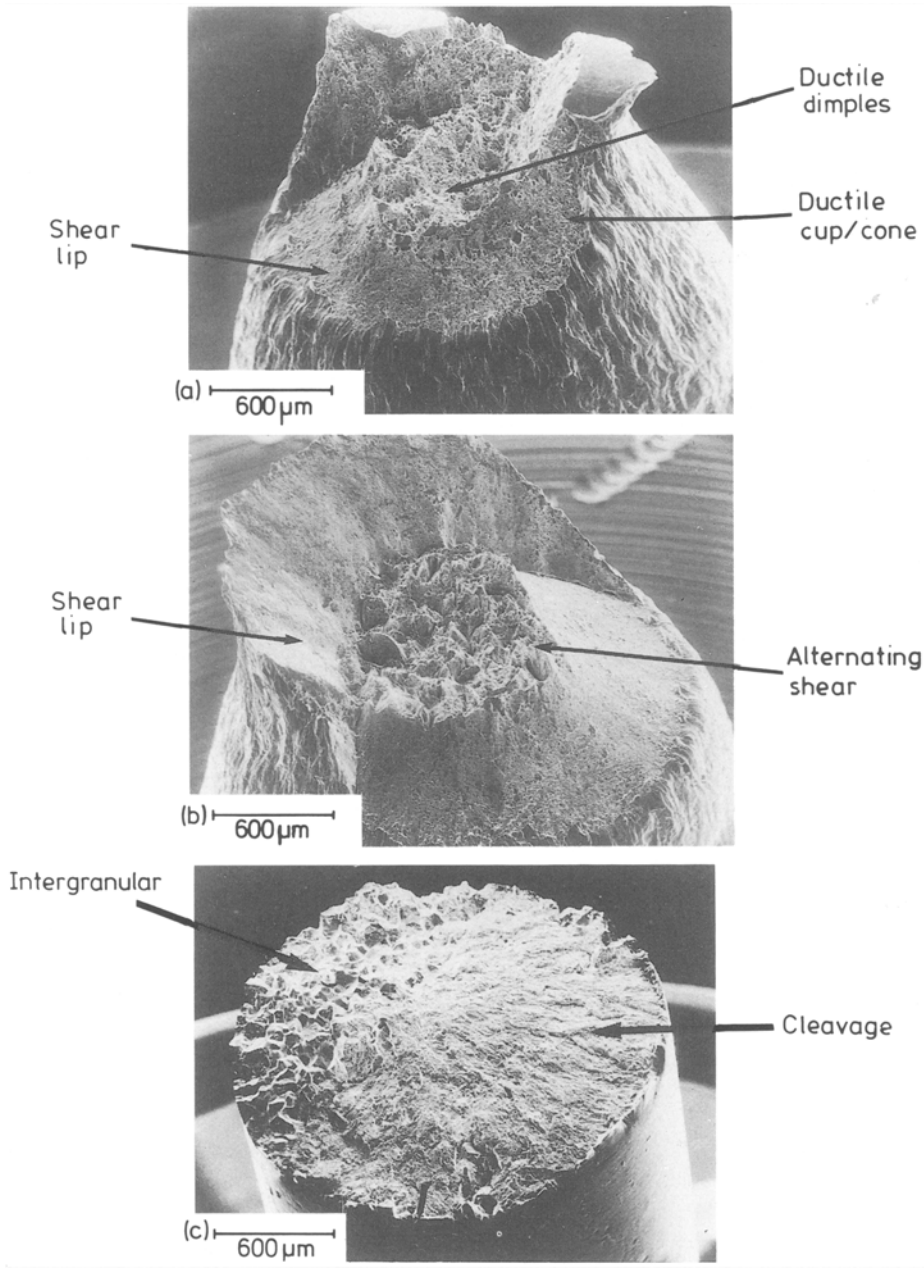

Figure 10 The effect of carbon concentration on the fracture of (a) Steel D, (b) Steel E, (c) Steel F, ice brine quenched from 1000 °C.

consequence of microvoid coalescence. The voids appeared to have been initiated first at the sparsely distributed inclusions (mainly MnS) since these were the sites of the deepest dimples on the fracture surface. The subsequent fracture of the inter-inclusion ligaments is believed to have occurred by further nucleation of voids at carbides, because the density and spatial distribution of microvoid dimples correlated with that of the carbide particles observed by metallography. Thus, for example, the pearlite/ferrite microstructures of furnace cooled steels resulted in a fracture in which some areas were densely covered in dimples (regions where fracture occurred in pearlite) separated by regions where few, if any dimples were found (regions where fracture occurred in ferrite). Steel E had fewer of these dimple-free regions, consistent with a reduced ferrite volume fraction.

The two most rapidly cooled conditions of Steel E together with the two most slowly cooled conditions of Steel F exhibited an "alternating shear" fracture in which the central region (of subcritical fracture prior to final catastrophic failure) had a zig-zag path formed by the intersection of alternating planes of shear failure. This intermediate mode of fracture is found in the regime between truly ductile and brittle fracture modes.

The faster cooling rates of the high carbon steel resulted in cleavage fracture at room temperature. For the three most rapidly cooled conditions, intergranular cleavage was first nucleated, and then underwent a transition to transgranular cleavage. The area of the intergranular mechanisms decreased with decreasing rate of cooling. The cleavage facets of the air cooled sample were heavily deformed and we refer to this as quasi-cleavage in Table V.

6. Discussion

The results of the acoustic emission experiments are summarized in the form of a map in Fig. 12 where, the

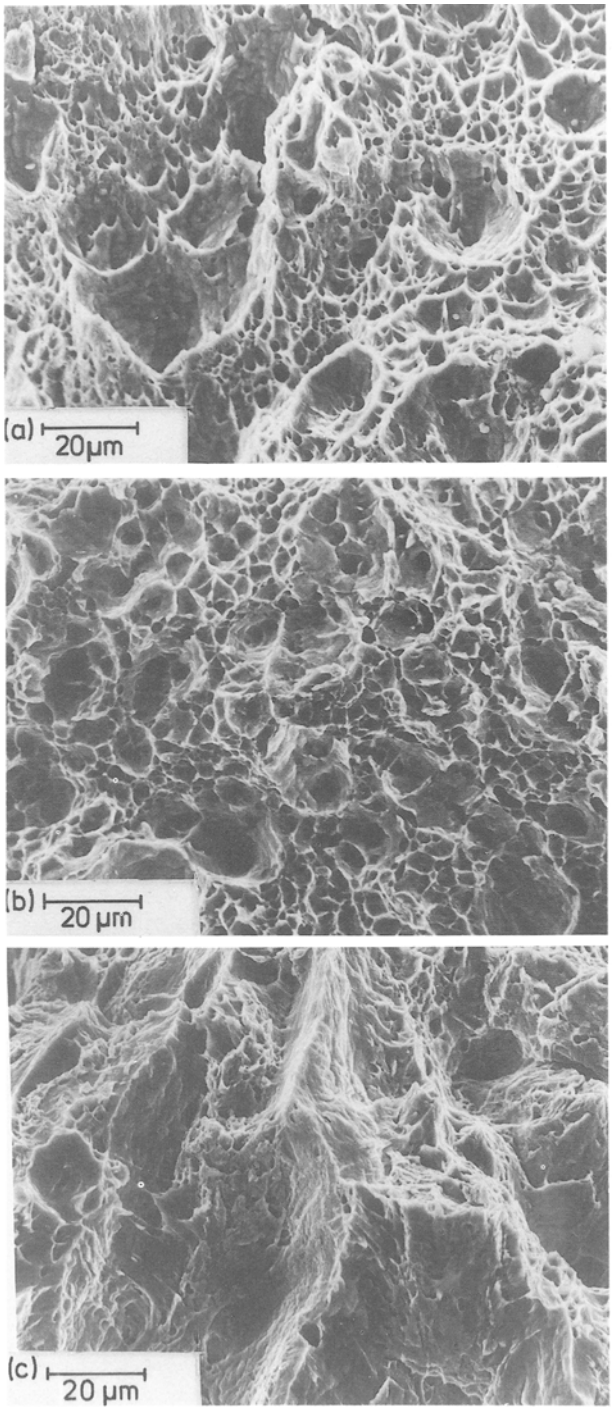

Figure 11 The effect of varying cooling rate on fracture mode of Steel D (a) oil quenched, (b) air cooled, (c) furnace cooled at $\approx 10\,^{\circ}\mathrm{C\,h^{-1}}$.

total emission energy is plotted on a cooling rate–carbon content map. It can be seen that acoustic emission from low alloy steels is strongly dependent upon carbon concentration and heat treatment. Some samples when strained, emit much detectable acoustic emissions, while others, often with only a slightly different microstructure, are found to emit little or even no detectable signals. This we believe is due to the controlling influence of the microstructure on the underlying micromechanisms of deformation and fracture responsible for acoustic emission.

6.1. Relationships between acoustic emission and source micromechanisms

An elastodynamic formulation has been developed to relate source micromechanics to the amplitude of acoustic emission signals [3, 23]. It represents the measured acoustic emission voltage as a convolution of the impulse response of the transducer and the sample with that of a source function. For longitudinal type transducers whose transfer function is fairly broadband, and for sources located directly beneath the transducer, the voltage signal corresponding to the first (longitudinal) wave arrival dominates the initially detected waveform [2]. Provided the transducer and sample geometry remain fixed it is then possible to deduce simpler relationships between signal amplitude and source stress–drop which is itself determined by the micromechanics of defect motion or phase change (e.g., martensitic transformation) [4]. For the mode I loading of tensile samples in the current experiments it is reasonable to assume that the most common microfracture will be the formation of (penny-shaped) mode I microcracks normal to the stress axis, while the most common plastic deformation process will be the expansion of glissile dislocation loops on a plane at 45° to the stress axis (on which the resolved shear stress is a maximum).

Then, it can be shown [4] that for a detectable signal to be emitted by a microcrack

$$\sigma a^2 v \geqslant 5 \times 10^{14} hx \quad \text{(Watts)} \tag{1}$$

where σ is the magnitude of pre-existing mode I stress, a, the radius of a penny-shaped crack, v, the radial velocity of crack propagation, h, the source-receiver distance and x, the smallest displacement detectable with the transducer (determined by background noise).

Similarly, it can be shown that for the expansion of a circular dislocation loop, the criterion for a detectable signal to be emitted is [4]

$$av \geqslant 7 \times 10^{13} hx \ (\mathrm{m^2\,s^{-1}}) \tag{2}$$

where a is the dislocation loop radius and v, the dislocation radial velocity.

These relationships establish criteria for signal detectability that depend upon (1) source parameters (local stress, σ, a and v), (2) distance of wave propagation (h), and (3) the noise-limited sensitivity of the detection apparatus (x). For the experiments reported here, $h = 40$ mm and $x = 10^{-14}$ m. Thus, microcracks are only detectable provided $\sigma a^2 v > 0.2$ watts and dislocations detected if $av > 0.3\ \mathrm{m^2\,s^{-1}}$.

It is well known that retained austenite may be stress-assisted to transform to martensite. Criteria for the detectability of acoustic emission from martensitic transformations have begun to be explored [22, 23]. The emission source can be likened to an inclusion undergoing an abrupt shape and elastic constant change. Then, the stress drop of the source, $\Delta\sigma(t)$ is given by

$$\Delta\sigma(t) = [\mathrm{I} + \Delta C D]^{-1}[(C + \Delta C)\beta^* - \Delta C \beta^{\circ}]\, V(t) \tag{3}$$

where I is the identity matrix, C, the stiffness tensor of

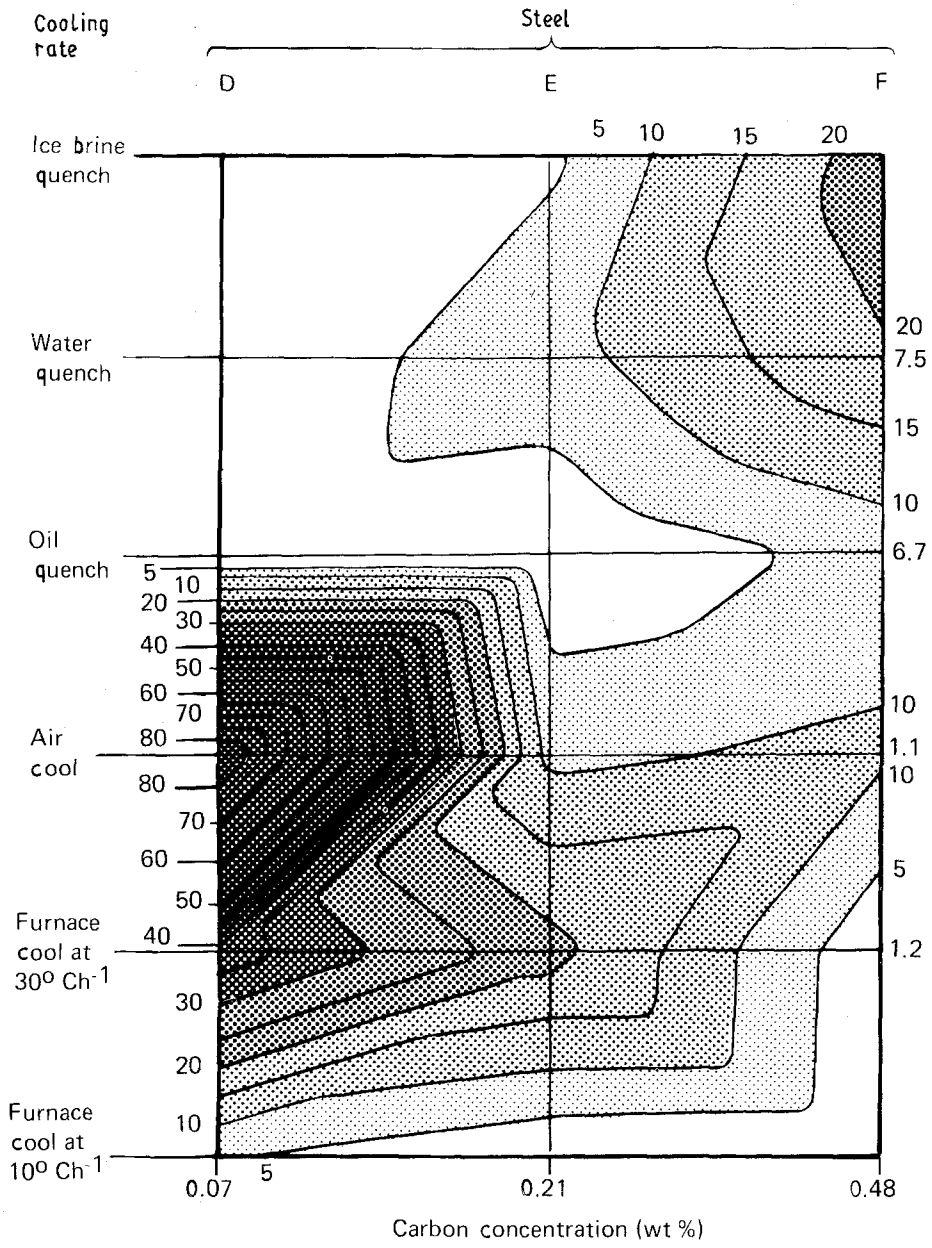

Figure 12 Map showing effect of cooling rate and carbon concentration on acoustic energy (mJ).

the parent (austenite) phase, $C + \Delta C$, the stiffness tensor of the transformed (martensite) phase, β^*, the unconstrained shape change of the transformation, β°, the pre-existing (residual) elastic strain, D, the shape matrix and $V(t)$, the time varying volume of martensite.

If $\Delta C \ll C$, and there is no residual strain field, Equation 3 reduces to

$$\Delta\sigma(t) \approx C\beta^* V(t) \quad (4)$$

Thus, the acoustic emission signal is proportional to the shape change and the volume of the transformation. Using the surface measurement data of Dunne and Bowles [24] for the shape change (β^*) associated with a martensitic transformation in a Fe–21% Ni–0.82% C alloy, and assuming a habit plane velocity of 2 mm^{-1} μs^{-1} it is shown [23] that the smallest detectable martensitic transformation would be the formation of an approximately 2 μm diameter spherical lath. Signal strength will increase proportionally with the magnitude of the shape strain and transformation volume.

Because the properties of defects controlling the generation of acoustic emission as expressed in the parameters (a, v) are difficult, if not impossible, to measure directly, validation of the above criteria is not possible. The best comparison is for studies of brittle fracture in iron and steels [14] in which acoustic emission and microcrack length were independently measured. The results could be reconciled with the above detectability criterion assuming a crack speed of 500–1000 ms^{-1} which is not an unreasonable velocity range for brittle fracture.

Verification for other microfracture processes and for slip relies on even less direct evidence. Recent reviews [1, 5, 23] have shown that the disappearance of acoustic emissions produced by slip processes during workhardening is consistent with the reduction of

the distance that glissile dislocations propagate before being pinned by sessile dislocations. Similar reductions in emission are found when grain boundary spacing is reduced. At the present time, it seems reasonable to use these criteria as a basis for the study of micromechanisms of deformation and fracture, although it must be recognized they provide only a general guide to the role of source parameters in generating detectable signals.

6.2. Acoustic emission and deformation micromechanisms

The microstructure was controlled in this study by heat treatment and variations of carbon content. Changes in microstructure influence the mechanisms of dislocation motion. In rapidly quenched samples, with a martensitic microstructure, the distance dislocations move is limited by the small width of the martensitic laths (≈ 1 μm). In addition, while the high initial dislocation density provides an abundance of potentially mobile dislocations, their mutual (forest) interaction restricts further the distance of propagation. The lack of a yield point on the stress–strain curves for these samples is consistent with many dislocations existing prior to deformation. The limited distance individual (or collective groups of) dislocations are able to move gives rise both to the high initial workhardening rate (Table IV), and to a failure of these steels to generate significant detectable acoustic emission during plastic deformation. It agrees with observations reported on other low alloy steels with similar microstructures [4].

In contrast the most slowly cooled samples have ferrite/pearlite microstructures. Their initial dislocation density is much lower. The yield stress of these microstructures has been found to fit a Hall–Petch model [9, 10], indicating that dislocations glide over a substantial fraction of the ferrite grain diameter at the start of deformation. Because of the relative scarcity of mobile dislocations, slip only begins when sufficient stress is applied to a source to cause dislocation multiplication. Then the created dislocations are able to glide rapidly at reduced stress across ferrite grains, resulting in a yield point, and the generation of a detectable acoustic signal. The special localization of this process to a band (Luders band) that first spreads over the cross-section and then gradually progresses along the gauge section [11], is the reason both for the prolonged stress plateau after yield on the stress–strain curve, and the persistence of many, individually weak, acoustic emission signals beyond the yield point.

Let us assume a typical event during this process to be a single dislocation that propagates from the centre to the edge of a grain to form an approximately circular dislocation loop (Fig. 13). The ferrite grain size of 0.07 %C steel was ≈ 60 μm. Thus, the radius of the largest dislocation loop in a ferrite grain would be ≈ 30 μm. The velocity of the dislocation is expected to be very high because of the large driving force (difference between applied stress and ferrite lattice drag stress); perhaps around 300 ms^{-1} (10% of the

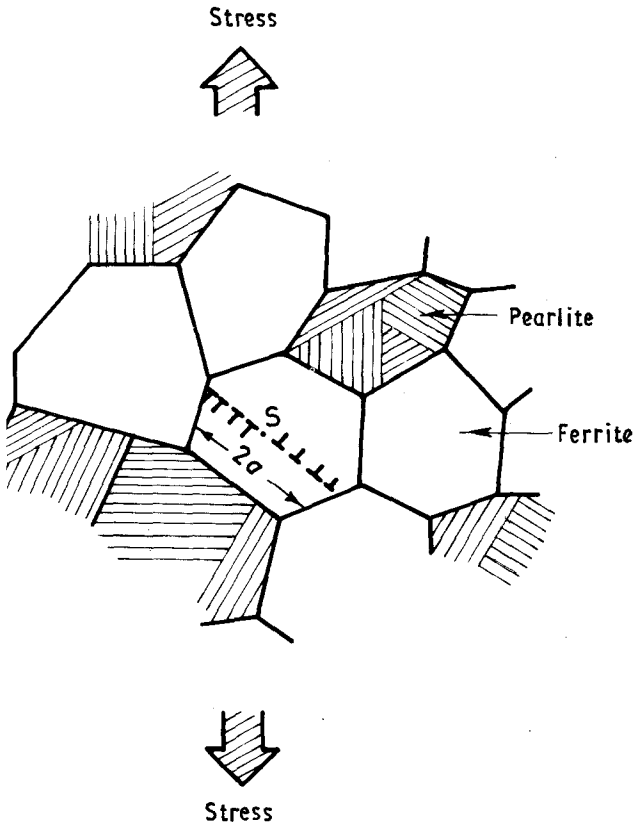

Figure 13 Model event during ferrite deformation. Dislocation at S expands until it reaches the ferrite grain boundary forming a loop of diameter 2*a*. Subsequent dislocations emitted at S form a grain boundary pile-up.

shear wave speed). Thus, $\dot{a}v \approx (30 \times 10^{-6}) \times (3 \times 10^{-2})$ $m^2 s^{-1} = 0.09\ m^2 s^{-1}$. This event would (by comparison with the detectability criterion) give rise to an acoustic emission signal about three times that of the noise background. The expanding dislocations which pile-up behind the leading dislocation could also enhance the signal. The complete process of forming a pile-up could increase the signal strength by an order of magnitude or more depending upon the coherence of the signals of each dislocation, the total number of dislocations emitted, and their dynamic (velocity) behaviour.

After initial yielding has progressed through the entire sample volume (at the end of the Luders plateau) further slip is incapable of generating detectable acoustic emission. This presumably arises because the conditions for unstable collective slip disappear with the emergence of a high mobile dislocation density. Now, the motion of many dislocations (each moving shorter distances and at slower velocity) satisfies the applied strain rate. Each dislocation's acoustic emission alone is too weak to be detected, and because the sources are randomly located (in space and time) their wavefields are incoherent, and the collective emission of all the many dislocations is still also not detectable.

The loss of acoustic emission in slow-cooled samples with increasing carbon content is consistent with a reduction both in the dimensions of the ferrite grains and the volume fraction of ferrite. It strongly suggests that both deformation and the fracture (if indeed it occurs at all at low strains) of cementite in

the pearlite is not a major source of detectable acoustic emission here since cementite volume fraction increases while the emission decreases with carbon content. Other work has shown that more coarse pearlites may fracture, and might be emission sources [12]. The fine cementite lamellar spacing (< 1 μm) in the pearlite here was probably the reason why slip in the intercementite ferrite lamellae was also impossible to detect. The suggestion [13] of an acoustic Barkhausen noise component to the acoustic emission cannot be discounted from the data reported here, but this usually is very weak and barely exceeds the background noise. Further experiments using simultaneously applied magnetic fields would be helpful in exploring this.

It is interesting to estimate the stress relaxation accompanying a typical slip event. The change in gauge length due to a dislocation loop expanding on a plane at 45 °C to the stress axis is

$$\Delta l = b(\alpha/A)\cos\theta \quad (5)$$

where α is the area of loop ($\pi \times 30^2 \times 10^{-12}$ m^2), A, the area of slip plane ($\pi \times 1.5^2 \times 10^{-6}$ m^2) and b, the Burgers vector.

For the typical situation considered here, $\alpha/A \approx 4 \times 10^{-4}$. Thus $\Delta l \approx 0.8 \times 10^{-14}$ m and the strain $\varepsilon \approx 0.2 \times 10^{-12}$. The accompanying stress relation $\Delta\sigma \approx 4 \times 10^{-2}$ Pa. This is far below the resolution of the load cells used during mechanical testing but is detectable acoustically indicating the extremely sensitive nature of acoustic emission measurements. The yield points observed on stress–strain curves must correspond to many hundreds or thousands of the events depicted in Fig. 13. Because quite strong acoustic emissions are observed, the dislocations responsible for the yield point must be moving in synchronism, and must be close to each other (compared with acoustic wavelength ≈ 6 mm at 1 MHz).

The sensitivity of acoustic emission to small stress relaxations is further illustrated in low carbon air cooled samples where intense acoustic emission is observed without any evidence of sudden microdeformations on the stress–strain curves. Some of the emission is presumably due to the stress assisted martensitic transformation (discussed below) of retained austenite in these two phase ($\alpha + \gamma$) structures. However, in the low carbon material, the ferrite boundary separations are up to 10 or 20 μm (Fig. 4a) enough for slip also to be able to generate relatively intense acoustic emission. The enhanced emission energy over the (slow cooled) ferrite/pearlite microstructure is consistent with the large volume fraction of ferrite in which dislocations could propagate distances of 10 to 20 μm and the additional signals from martensitic transformations. The higher yield strength of this condition may also have contributed to the enhanced emission by increasing the dislocation velocity.

6.3. Acoustic emission from martensitic transformation

Air cooling the low carbon steel resulted in a two phase ($\alpha + \gamma$) microstructure due to the relatively prolonged period of cooling above the eutectoid temperature. The retained austenite is of the "blocky" morphology similar to that reported by Rao et al. [25] with dimensions up to 10 μm. Much of this retained austenite has been reported to undergo a transformation to martensite during the first few per cent strain [26, 27]. Earlier it was shown that detectable emissions are generated by martensitic transformations provided the volume transformed has a dimension greater than about 2 μm. The very intense emission activity of the air cooled low (and to a lesser extent medium) carbon steel (Fig. 8a) is believed to be due to this additional emission source. The difference in the emission energy of different samples then depends upon the volume fraction of retained austenite with a dimension greater than approximately 2 μm, and this is very sensitive to cooling rate and composition.

Retained austenite is also present in high carbon samples subjected to air cooling and, indeed more rapid quenching [28]. The austenite in this case, however, is distributed as a thin (0.01 μm) film between individual martensite plates/laths [29]. It is unclear if this austenite martensitically transforms upon straining, but in the event that it does, the very small volume involved in a given transformation would be unlikely to result in a detected event.

6.4. Acoustic emission and fracture micromechanisms

The samples tested underwent fracture by one of three modes: cleavage, alternating shear or ductile dimple fracture (Table V). The micromechanisms of each mode are quite different and the acoustic data reflect this. What can we learn from the acoustic emission data during each type of fracture?

From SEM, the highest proportion of brittle fracture was found in the high carbon steels in rapidly cooled states. Even though the samples fractured during nominally elastic loading, indicating brittle behaviour, the first emission, and thus the first microcracking, occurred at loads almost an order of magnitude below that required to cause final fracture. The low load emissions are most probably identifiable with the region of intergranular crack growth evident in the fractographs. Previous work using quantitative acoustic emission techniques indicated that this mechanism of microfracture involved intermittent crack propagation typically over a distance of three to five grain facets before arrest [14]. Since there are 200 to 300 exposed grain boundaries on the fractograph (Fig. 10c), it is anticipated that about 50 acoustic emissions would be generated by this process if every grain boundary contributed to emission. Within the limits of the estimation, this corresponds to the number of signals detected prior to catastrophic fracture.

Fractography also indicated that final fracture proceeded by a transgranular cleavage process initiated at the edge of the intergranular region. No arrest marks were evident on the fracture surface indicating that failure progressed in an unstable manner as one event, tending to confirm that most, if not

all, of the acoustic emission signals originated from intergranular crack advance. The decrease in acoustic emission for the more slowly cooled high carbon steels corresponded to a decrease in the number of intergranular facets observed on the fracture surface as the sample ductility increased.

An alternating shear mechanism of fracture predominated in some samples, particularly the ice-brine and water-quenched medium carbon material, Table V. These specimens also generated appreciable acoustic emission. The plastic deformation was highly localized as well as being unstable and occurred as a rapid shear fracture mode (on a plane at $\approx 30°$ to the tensile axis) just beyond maximum load (Fig. 6). This is typical of ductile fracture in high-strength steels in which workhardening capacity is exhausted, although in more highly constrained geometries, such as the tip of a notch, the fracture generally follows a zig-zag path on planes at about 45° to the applied stress axis [15–21].

A basic feature of this type of fracture is plastic collapse of the inter-inclusion ligaments resulting in highly localized deformation bands on the plane of maximum resolved shear stress [30]. Within these deformation bands the local strain can be extremely high (> 1) and once a critical void fraction is reached, this can lead to the formation of void sheets (often nucleated at small particles) which can rapidly coalesce to give ligament separation. This process is consistent with the topography of the fracture surfaces, which were covered with an array of shallow dimples, usually centred on small inclusions, and a lower subfracture surface void density.

The rapidly quenched samples that exhibited alternating shear were "acoustically noisy" presumably because large areas of the matrix underwent rapid fracture under a high fracture stress, which results in large and abrupt stress relaxations. For example, shear facets were typically 150 μm in length and the detectability criteria indicate that even quite slow crack velocities ($\approx 50\ ms^{-1}$) would give energetic signals well above background. The number of shear facets correlates quite well with the number of signals from the rapidly cooled samples again indicating that the formation of each facet generates a detectable signal.

The alternating shear process in the high carbon slowly cooled samples is different from that of the rapidly cooled samples of medium carbon content, in that less acoustic emission accompanied fracture in the latter. The greater workhardening capacity of inter-inclusion/inter-carbide ligaments in this case would result in a less rapid form of shear failure, and the shear instability is avoided.

In contrast to the brittle modes of fracture, virtually no emission was observed from the majority of the samples which fractured by a ductile void-coalescence process. The deepest dimples (those considered to form earliest during plastic flow) appeared to have formed at the rather sparsely distributed MnS inclusions. The distribution of the inclusions was independent both of quench rate and carbon concentration. Between the MnS nucleated voids, finer dimples, apparently nucleated on carbides were also present. These smaller voids grew steadily during post maximum stress deformation and interlinked to form an internal microcrack. Microcracks eventually also interlinked to form a centrally located flaw that raised the stress intensity in the uncracked ligament sufficiently to cause a shear instability and catastrophic sample fracture. With the exception of the last process none of these processes in any of the wide range of microstructures undergoing ductile-dimple fracture generated any detectable acoustic emission. This is presumably because they all occur slowly (so there is no mechanical instability) and the ligament separations occur over such small areas that the small stress relaxation is below the detection threshold.

7. Conclusions

1. Only in microstructures in which a ferrite dimension exceeds 10 μm, is dislocation motion observed to generate detectable acoustic emission during plastic deformation. In the steels examined here, this criterion is best met as the carbon content and cooling rate are reduced.

2. Intermediate cooling rates resulted in a dual phase ($\alpha + \gamma$) microstructure in low carbon steel. Subsequent straining generated very intense acoustic emissions, believed to be associated with a combination of martensitic transformations of the retained austenite and slip in the ferrite.

3. When intergranular crack advance takes place this is the most readily detectable fracture process in these steels. This fracture process is confined to high carbon alloys with a martensitic microstructure.

4. The alternating shear mechanism of fracture can be an energetic emission source in rapidly cooled material, indicating this process occurs at a velocity $> 50\ ms^{-1}$ in low workhardening capacity matrices.

5. Ductile dimple fracture, the most common mechanism of crack advance in bainitic and pearlitic microstructures at ambient temperatures, generates no detectable acoustic emission, consistent with the view that it occurs under quasi-static conditions.

Acknowledgements

We wish to extend our appreciation to Drs B. L. Eyre, B. Pickering and J. Hudson for stimulating discussions of this work and to P. Lane and A. Bartlett for the practical assistance rendered. This work was funded by MOD (Procurement Executive) through AMTE Holten Heath.

References

1. H. N. G. WADLEY, C. B. SCRUBY and J. H. SPEAKE, *Int. Met. Rev.* **25** (1980) 41.
2. C. B. SCRUBY, H. N. G. WADLEY and J. J. HILL, *J. Phys. D.: Appl. Phys.* **16** (1983) 1069.
3. J. A. SIMMONS and R. B. CLOUGH, in Proceedings of the Conference on Dislocation Modelling of Physical Systems, Gainesville, FL, 1980 (Pergamon).
4. C. B. SCRUBY, C. JONES, J. M. TITCHMARSH and H. N. G. WADLEY, *Metal Science*, June (1981) 241.
5. H. N. G. WADLEY and R. MEHRABIAN, in Proceedings Symposium Nondestructive Methods for Material Property Determination, Hershey, PA, April 6–8, 1983.

6. C. B. SCRUBY and H. N. G. WADLEY, *Progress in Nuclear Energy* **11** (1983) 275.
7. P. G. BENTLEY, E. J. BURTON, A. COWAN, D. G. DAWSON and T. INGHAM, in Proceedings of 2nd Int. Conference, Press Vessel Techn., (ASME, New York, 1973), p. 643.
8. H. N. G. WADLEY, C. B. SCRUBY, P. LANE and J. A. HUDSON, *Metal Science* **15** (1981) 514.
9. N. J. PETCH, *J. Iron and Steel Inst.* **174** (1953) 25.
10. E. O. HALL, in *Proc. Phys. Soc. Lond.* **64** (1951) 747.
11. H. FUJITA and S. MIYAZAKI, *Acta Met.* **20** (1978) 1273.
12. A. N. HADJICOSTIS and S. H. CARPENTER, *Mat. Eval.* **Feb.** (1980) 19.
13. F. HIGGINS, PhD Thesis, Denver University (1977).
14. H. N. G. WADLEY, C. B. SCRUBY and G. SHRIMPTON, *Acta Met.* **29** (1980) 399.
15. G. CLARK and J. F. KNOTT, *Met. Sci.* **11** (1977) 531.
16. F. A. McCLINTOCK, S. M. KADLAN and C. A. BERG, *Int. J. Fract. Mech.* **2** (1966) 614.
17. I. E. FRENCH and P. F. WEINRICH, *Metall. Trans.* **7d** (1976) 1841.
18. C. D. BEACHEM and G. R. YODER, *ibid.* **4** (1973) 1145.
19. G. GREEN and J. F. KNOTT, *J. Engng Mater. Technol.* **Jan** (1976) 37.
20. G. G. SAUNDERS and J. F. KNOTT, *Welding Inst. Res. Bull.*, **April** (1975) 106.
21. J. Q. CLAYTON and J. F. KNOTT, *Met. Sci.* (1976) 63.
22. J. A. SIMMONS and H. N. G. WADLEY, in "Wave propagation in homogeneous media and nondestructive evaluation", edited by G. C. Johnson, AMD-62 (ASME, New York, 1984) p. 51.
23. H. N. G. WADLEY and J. A. SIMMONS, in "Handbook on emission", edited by R. K. Miller and P. McIntyre, ASNT (1988) p. 63.
24. D. P. DUNN and J. S. BOWLES, *Acta Metall.* **12** (1969) 201.
25. NAVASHIMA-RAO, V. BANGARU and A. K. SACHDEV, *Met. Trans. A*, **13d** (1982) 1899.
26. A. K. SACHDEV, *Acta Metall.* **31** (1983) 2037.
27. T. FURUKAWA, H. MORIKAWA, H. TAKECHI and K. KOYAMA, in "Structure Properties of Dual Phase Steels", edited by R. A. Kot and J. W. Morris (AIME, New York, 1979) p. 281.
28. G. R. SPEICH, *Met. Trans. A*, **3** (1972) 1045.
29. R. W. K. HONEYCOMBE, in "Steels-microstructure and properties" (ASM, Metals Park, OH, 1981) p. 151.
30. A. NEEDLEMAN and V. TVERGAARD, in "Finite elements, special problems in solid mechanics", Vol. 5, edited by J. T. Oden and G. F. Carey (Prentice-Hall, 1984) p. 94.

Received 29 June 1990
and accepted 31 January 1991